The Mid-Infrared Instrument for the *James Webb Space Telescope*, IX: Predicted Sensitivity

Alistair Glasse,[1] G. H. Rieke,[2] E. Bauwens,[3] Macarena García-Marín,[4] M. E. Ressler,[5] Steffen Rost,[4] T. V. Tikkanen,[6] B. Vandenbussche,[3] and G. S. Wright[1]

ABSTRACT. We present an estimate of the performance that will be achieved during on-orbit operations of the *JWST* mid-infrared instrument, MIRI. The efficiency of the main imager and spectrometer systems in detecting photons from an astronomical target are presented, based on measurements at subsystem and instrument-level testing, with the end-to-end transmission budget discussed in some detail. The brightest target fluxes that can be measured without saturating the detectors are provided. The sensitivity for long-duration observations of faint sources is presented in terms of the target flux required to achieve a signal-to-noise ratio of 10 after a 10,000 s observation. The algorithms used in the sensitivity model are presented, including the understanding gained during testing of the MIRI flight model and flight-like detectors.

Online material: color figures

1. INTRODUCTION

MIRI has been designed (Wright et al. 2014, hereafter Paper II) to detect as much as possible of the signal from the astronomical target collected by the *James Webb Space Telescope (JWST)* primary aperture, and so the measurement noise would be limited to the statistical fluctuations on the total signal (target plus background), commonly referred to as shot noise. In practice, the nonideal behavior of optics and detector systems mean that this goal can be closely approached, but never reached: not all light collected by the telescope is detected, and at the short wavelength end of MIRI's spectral range detector dark current becomes significant, most notably for the medium-resolution spectrometer. The contributions of the opto-electronic subsystems to MIRI's sensitivity have been carefully characterized during the instrument build, by direct measurement at component level combined with system-level analysis, and culminating in extended cryogenic testing of the fully assembled MIRI flight model at the Rutherford Appleton Laboratory (RAL) during

2011, in a flight-like radiative environment using a well characterized radiometric source (the MIRI Telescope Simulator, MTS, discussed in Paper II). Our understanding of the detector performance (Rieke et al. 2014, hereafter Paper VII) has benefitted from an extensive program of performance testing conducted using flight-like detectors at JPL.

These performance metrics were brought together in a sensitivity model that was formulated early on in the project (Swinyard et al. 2004). This has since been extended and refined to track the impact of developments to the observatory design on MIRI's expected on-orbit performance and to include the knowledge gained during the MIRI build and test phases. It includes performance estimates at all wavelengths and optical configurations.

In this paper, we present and justify the parameters and algorithms that comprise the sensitivity model, and present its predictions for three of MIRI's four major operational configurations; the imager, the low-resolution spectrometer (LRS), and the medium-resolution integral field spectrometer (MRS). Coronagraphy is not included because its performance is more dependent on contrast and rejection than on throughput and sampling, as dealt within this paper. The predicted coronagraph performance is discussed in Boccaletti et al. (2014; Paper V).

The results presented here should be interpreted as the limiting sensitivities that could be achieved during long-duration (hour-long or more) staring observations made at a single spacecraft pointing. They exclude inefficiencies due to the operational overheads described in Gordon et al. (2014; Paper X), such as target acquisition, small-angle maneuvers to allow efficient background subtraction, time spent moving MIRI mechanisms or taking calibration observations.

[1] UK Astronomy Technology Centre, Royal Observatory, Edinburgh, Blackford Hill, Edinburgh EH9 3HJ, United Kingdom.

[2] Steward Observatory, 933 N. Cherry Avenue, University of Arizona, Tucson, AZ 85721.

[3] Institute of Astronomy KU Leuven, Celestijnenlaan 200D, 3001 Leuven, Belgium.

[4] I. Physikalisches Institut, Universität zu Köln, Zlpicher Strasse 77, 50937 Köln, Germany.

[5] Jet Propulsion Laboratory, California Institute of Technology, 4800 Oak Grove Drive, Pasadena, CA 91109.

[6] Department of Physics and Astronomy, University of Leicester, University Road, Leicester LE1 7RH, United Kingdom.

2. MODEL COMPONENTS

2.1. The *JWST* Observatory

The massive gains in sensitivity that MIRI will achieve, compared to current and planned mid-infrared instruments, are primarily due to the large ($25\ \mathrm{m}^2$) collecting area and the cold (40 K) radiative environment provided by the *JWST*. When compared to ground-based observatories, the absence of atmospheric absorption bands and thermal emission from both the atmosphere and telescope makes *JWST* more than competitive even with the 30 and 40 m class telescopes now being planned.

At the short wavelength end of MIRI's spectral range around 5 μm, the remaining radiative background signal is dominated by emission from the zodiacal dust concentrated in the ecliptic plane; longward of 17 μm or so, stray light from the observatory sunshield and the thermal emission of the telescope optics become dominant.

For the purposes of sensitivity modeling, we represent the backgrounds by the sum of six gray-body emission spectra, whose emissivities and effective temperatures are listed in Table 1, with spectral energy distributions plotted in Figure 1, where the background spectrum is seen to rise steeply across MIRI's spectral range.

Components A and B in Table 1 are fits to the scattered and emissive components of the zodiacal dust spectrum toward the celestial north pole (Wright 1998), scaled by a factor of 1.2 to be representative of typical pointing scenarios. Components C–F are derived from a fit to a detailed straylight model of the observatory background (Lightsey & Wei 2012), such that individual terms should not be identified as being physically representative of any specific observatory subsystem. This particular model gives a total of 188 MJy sr^{-1} at 20 μm, just under the second-level requirement of 200 MJy sr^{-1}.

To include the thermal background from the telescope, components A–F are summed together to give the background spectrum that is plotted as the thick solid line labeled "TOTAL" in Figure 1. As a contingency, we also show the result of doubling

TABLE 1
GRAY-BODY COMPONENTS OF THE BACKGROUND MODEL
USED FOR SENSITIVITY CALCULATIONS

Component	Emissivity	Temperature (K)
A	4.20×10^{-14}	5500
B	4.30×10^{-8}	270
C	3.35×10^{-7}	133.8
D	9.70×10^{-5}	71.0
E	1.72×10^{-3}	62.0
F	1.48×10^{-2}	51.7
(G)	1.31×10^{-4}	86.7

NOTE.—Components A and B are fits to the scattered and emissive components of the zodiacal dust spectrum, while C–F represent the observatory straylight. See the text for a more detailed explanation of the terms.
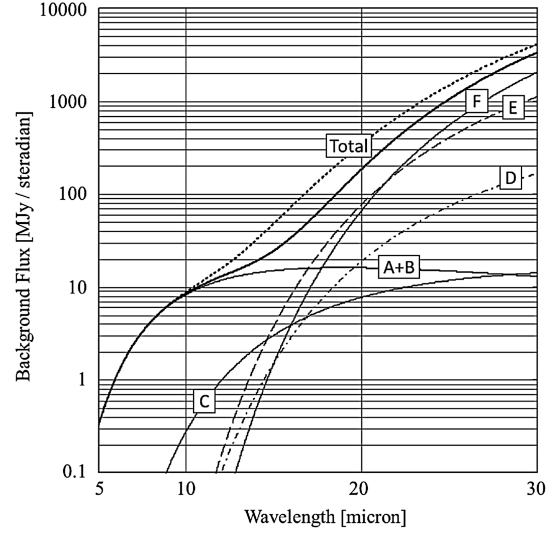

FIG. 1.—Background emission spectra used in MIRI sensitivity modeling.

the current estimates of facility emission by adding an additional component (*G* in Table 1) with the effect of increasing the background flux at $\lambda = 20$ μm to 350 MJy steradian^{-1}.

In interpreting Figure 1, it may be helpful to note that for the MIRI imager pixel scale of $0.11''$, the usable area of the *JWST* entrance pupil ($A_{\mathrm{tel}} = 25.03\ \mathrm{m}^2$) and the nominal transmission of the telescope optics up to the MIRI entrance focal plane ($\tau_{\mathrm{tel}} = 0.88$ at the start of the mission), a flux of 0.4 MJy sterad^{-1} at $\lambda = 5$ μm corresponds to 7.5 photon s^{-1} pixel^{-1} in a 1 μm pass-band. At $\lambda = 20$ μm, a flux of 188 MJy sterad^{-1} equates to 890 photon s^{-1} pixel^{-1} μm^{-1}.

2.2. Photon Conversion Efficiency

The photon conversion efficiency (PCE) is defined as the fraction of photons crossing the MIRI focal plane within the science field of view that are detected (and so contribute to the measurement). It appears in the following formula describing the photocurrent i generated in a detector pixel by a photon flux entering the telescope, $P(\lambda)$ (with units of photon steradian^{-1} micron^{-1}):

$$i = \Omega_{\mathrm{pix}} \tau_{\mathrm{tel}} \tau_{\mathrm{EOL}} \int_{\Delta\lambda} P(\lambda) \tau_\lambda \eta_\lambda d\lambda. \qquad (1)$$

Here, the PCE is written as the product of the optical transmission of all elements from the focal plane to the detector τ_λ, with the detector quantum efficiency η_λ (measured in detected electrons per incident photon). The factor Ω_{pix}, which represents the solid angle field of view of a single pixel, is combined with two additional wavelength independent transmission terms; τ_{tel} (set equal to 0.88) describes the transmission of the clean telescope optics at the start of the mission, and τ_{EOL} (set equal to 0.80) is then used to account for the loss in transmission of all elements

in the optical train up to the "end-of-life" of the nominal 5-year mission.

We determined the "beginning of life" PCE in two independent ways, with the results for the imager shown in Figure 2 and for the MRS shown in Figure 3. For the first method, the measured and estimated transmission efficiencies due to all elements in the optical train were combined with the partly measured, partly modeled, detector quantum efficiencies given in Paper VII, to generate bottom-up wavelength-dependent PCE profiles for the imager, LRS and MRS. These profiles are plotted as the solid lines in Figures 2 and 3.

In the case of the imager, the wavelength-dependent transmissions of the band selection filters were measured at the 7 K operating temperature by the filter manufacturers (University of Reading and Spectrogon). The seven gold-coated mirrors in the optical train from the entrance focal plane were then allocated a reflectivity of 0.98 per surface (consistent with cryogenic measurements made on similar mirrors). An additional transmission factor of 0.8 was applied to the end-to-end transmission to allow for contamination up to the start of the mission (i.e., independent of the end-of-life factor τ_{EOL} referred to above).

For the MRS (whose optical train is described in Wells et al. [2014], hereafter Paper VI), the transmissions of the dichroic filters were again derived from the manufacturer's (University of Reading) cryogenic measurements. The same reflectivity figure of 0.98 was used for the mirrors, where we note that the number of mirrors in each of MRS Channels 1–4 is 26, 25, 24, and 29, respectively.

As discussed in Paper VI, the optical design of the MRS was tailored to minimize losses due to diffraction, primarily by oversizing optical elements lying between the integral field units and the detectors. However, some losses were expected to remain, so modeling (using the *GLAD* software package) was used to derive effective transmissions τ_{MRS_diff} at the short and long wavelength ends of each MRS channel, accounting for diffraction losses. These transmissions are tabulated in Table 2.
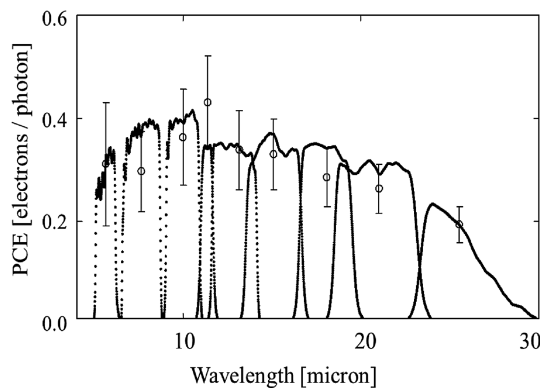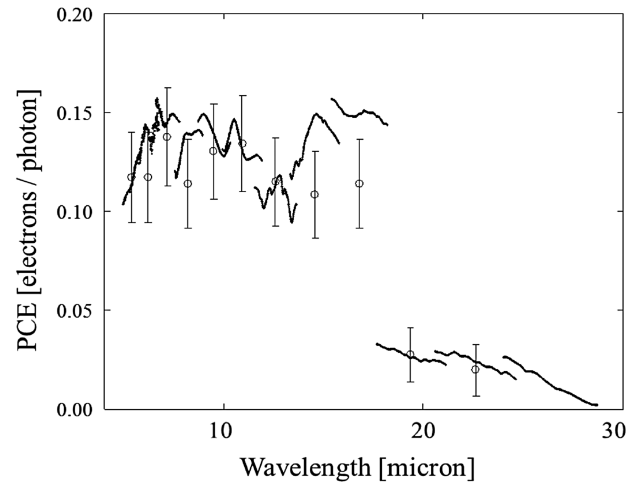

FIG. 3.—Photon conversion efficiency (units of e photon^{-1}) of the MIRI Medium-Resolution Spectrometer.

For use in the sensitivity model, the value of τ_{MRS_diff} at a specific wavelength was derived by linear interpolation.

The efficiency of the diffraction gratings was set to be 0.6, based on modeling (using *PCGrate*) for all gratings in Channels 1, 2, and 3. For Channel 4, lower than expected efficiency was measured during testing at RAL (see Paper VI). This was accounted for in the sensitivity model by setting the grating efficiencies in this case equal to 0.17.

The product of the above transmissions and efficiencies, with the same additional end-to-end factor of 0.8 as used for the imager to account for beginning of life contamination, is then plotted as the solid line in Figure 3.

A second method for estimating the PCE independently of the subsystem budgets described above involved direct measurement of the signal during observations of the extended source of the MIRI telescope simulator (MTS) during flight model testing at RAL in 2011. An end-to-end model of the photometric output of the MTS (called MTSSim), described in Paper II, was then used to provide an absolute flux calibration of these measurements, with a value of 5.5 electrons per data number assumed for the electronic gain of the detector system (Ressler et al. [2015]; Paper VIII). These band averaged results are plotted in Figures 2 and 3 as points with error bars. We note

FIG. 2.—Photon conversion efficiency (detected electrons per photon crossing the MIRI Imager entrance focal plane).

TABLE 2

EFFECTIVE TRANSMISSION DUE TO DIFFRACTIVE LOSSES AT THE SHORT AND LONG WAVELENGTH LIMITS OF THE FOUR MRS CHANNELS

Channel	τ_{MRS_diff} at λ_{short}	τ_{MRS_diff} at λ_{long}
1	0.95	0.91
2	0.94	0.91
3	0.92	0.87
4	0.92	0.86

that it was necessary to scale the PCE values predicted by *MTSSim* (version 2.2) by a factor of 0.55 for both the imager and MRS to obtain the reasonable agreement with the MIRI subsystem derived profiles seen in Figures 2 and 3. This factor was ascribed in Paper II to systematic errors in *MTSSim*; we note here that one alternative, namely that the MIRI subsystem determined PCEs presented here are all systematically too low by a factor of 0.55, is felt to be unlikely; it is difficult to identify a single component common to both the MRS and the imager that could credibly have a transmission that is almost a factor of 2 higher than the values described above.

2.3. Encircled Energy

Not all of the signal detected from a point-like astronomical target will contribute to the photometric measurement. The signal is distributed over many pixels due to image broadening by diffraction, by the telescope and instrument optics, and by scattering and crosstalk in the detector itself (Paper VII). This broadening, which is quantified as the instrument point-spread function (PSF), forces us to make a trade, which maximizes the fraction of the total integrated signal from the target that is sampled, whilst minimizing the number of pixels contributing noise.

If we consider the target as a point source of total integrated flux $F_{\text{point\_tgt}}$ (Jansky), then the photon flux (in units of photon s^{-1} μm^{-1} arcsec^{-2}) contributing to the measured signal can be calculated in terms of the fraction f_{phot} of the total falling within a circular photometric aperture of radius r_{phot}, containing N_{phot} pixels, each of which views a solid angle on the sky equal to Ω_{pix}:

$$P_{\text{point\_tgt}} = \frac{F_{\text{point\_tgt}} f_{\text{phot}}}{\Omega_{\text{pix}} N_{\text{phot}}} \frac{A_{\text{tel}}}{h\lambda}. \qquad (2)$$

Testing of the MIRI flight model has shown that the images delivered to the detector by the MIRI optics at wavelengths longward of $\lambda = 7$ μm are near-diffraction-limited, allowing us to make a straightforward definition of the photometric aperture radius, r_{phot}, as being equal to that of the first dark Airy ring. For the *JWST*'s noncircular pupil, we approximate this as:

$$r_{\text{phot}} = 0\overset{''}{.}42 \left(\frac{\lambda}{10 \ \mu\text{m}} \right). \qquad (3)$$

We choose to express the encircled energy fraction, f_{phot} as the product of two factors: f_{opt}, which describes the effects of image broadening due to misalignment (primarily defocus) between MIRI and the *JWST*, and f_{det} which accounts for the flux lost outside the photometric aperture due to scattering in the detector (see Fig. 4).

The physical origin and impact on the image quality of scattering within the detector are described in Paper VII. For inclusion in the sensitivity model we represent this effect with the function,

$$f_{\text{det}} = 1 - a_{\text{det}} e^{-([\tau_1 + \tau_2](\frac{\lambda}{7\mu m})^2)}. \qquad (4)$$

Here the factor τ_1 (equal to 0.36) is the optical depth at $\lambda = 7$ μm for absorption by a single pass through the 35 μm thick active layer of the MIRI detector for light at normal incidence, as defined in Paper VII. In the simple case when factors $a_{\text{det}} = 1$ and $\tau_1 = 0$, f_{det} would then model the case where all light that is not absorbed within the active layer on the way in is lost from the photometric aperture. The factors τ_2 and a_{det} then refine this picture to better fit two features of the scattering as measured during flight model testing.

First, as described in Bouchet et al. (2014, Paper III), the measured dimensions of the imager PSF are close to the expectations of diffraction limited performance. Detailed optical modeling then allowed an upper limit to be placed on the fraction of light scattered to large radii (i.e., outside the photometric aperture) equal to 15% for the F560W filter. This constraint is satisfied by setting a_{det} equal to 0.32. We might interpret a_{det} as a measure of the wavelength independent component of the scattered light.

The second observed feature of the detector scattering, embodied in factor τ_2 comes from flood-illuminated images measured during the RAL test campaign. It was found that the stray light falling on regions of the imager occulted by the focal plane mask (Paper III) could be well modeled by the expected diffraction limited PSF at wavelengths longward of 10 μm, but that for the F560W and F770W filters an additional component was needed, which was ascribed to detector scattering. The amplitude of this component (which equates to $1 - f_{\text{det}}$) was found to be a factor of 2 larger for the F560W filter than for F770W. Matching this ratio for $\tau_1 = 0.36$ requires that $\tau_2 = 0.85$.

The functional similarity between τ_1 and τ_2 should not be interpreted as implying a similar physical origin. As discussed in Paper VII, the details of the scattering process are complicated; our aim in equation (4) is simply to provide a representation of its coarse behavior suitable for inclusion in the sensitivity model.

For ideal optical performance (a Strehl ratio of 100%) and perfect optical alignment between MIRI and the telescope, r_{phot} will encircle a fraction $f_{\text{optA}} = 70\%$ of the flux for a point-like target. Optical modeling of MIRI on the *JWST* has allowed us to derive values for f_{opt} (with an estimated error of $\pm 1\%$) under a range of nonideal conditions of defocus and pupil shear misalignment. The worst-case f_{optB} occurs where the optical train (MIRI plus telescope) introduces a wavefront error equivalent to an 85% Strehl ratio, on top of which there is 5 mm of defocus and 2% pupil decenter between the focal plane delivered by the *JWST* and that accepted by MIRI. This function is well described by,

$$f_{\text{optB}} = 0.68 \left[1 - \left(\frac{2.47 \ \mu\text{m}}{\lambda} \right)^{1.8} \right]. \qquad (5)$$
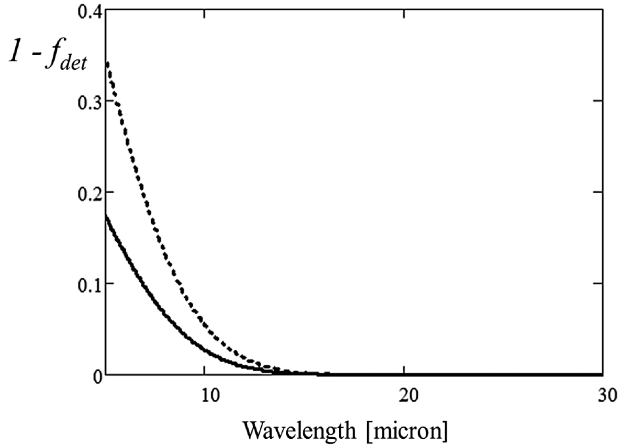
FIG. 4.—The fraction of light lost from the photometric aperture due to detector scattering as a function of wavelength: the imager is shown as a *solid line* and the MRS as a *dashed line*.

The limits on f_{phot} for the imager set by these best and worst-case bounds on f_{opt} are plotted as the dotted lines in Figure 5.

Measurements of the coalignment between the MIRI flight model and the *JWST*-ISIM instrument module showed that the defocus and pupil decenter were both consistent with the case of "perfect" optical alignment, whilst the measured image quality suggested that the delivered Strehl ratio at the detector was in excess of 95%. We therefore, chose to retire a substantial fraction of the risk associated with these optical effects by adopting a weighted sum of the limiting cases,

$$f_{opt} = 0.75 f_{optA} + 0.25 f_{optB}. \qquad (6)$$

It is this function that was used to generate the encircled energy fraction $f_{phot} = f_{det} \times f_{opt}$ in the sensitivity model and that is plotted for the imager and LRS in Figure 5.
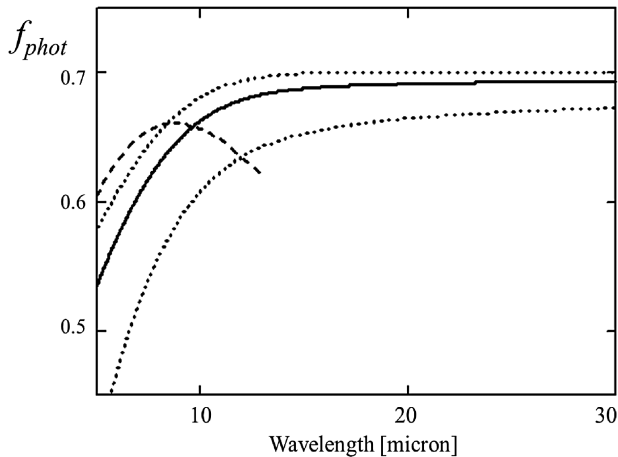
We must adapt this approach for the low-resolution spectrometer (the LRS, described in Paper IV), and the medium-resolution spectrometer (the MRS, described in Paper VI) as a result of the differences in the dimensions of their respective photometric apertures.

For the LRS, the aperture is assumed to be rectangular, with dimensions equal to the slit width ($0.51''$, or 4.6 pixels) in the across-slit direction and by r_{phot} in the along slit direction. The spectral resolution in terms of pixels is shown in Figure 6. We then need to modify the form of f_{phot} to account for the change in encircled energy fraction due to the noncircular aperture. Numerical integration of the nominal PSF was used to determine a correction factor, equal to the ratio of the energy within the rectangular LRS aperture to the circular aperture defined by r_{phot}, normalized at $\lambda = 10$ μm. This was found to be well fitted (maximum deviations <0.01) by a linear function, which generates correction factors for f_{phot} that vary from 1.13 at $\lambda = 5$ μm to 0.85 at $\lambda = 15$ μm.

For the MRS, we note that the photometric aperture is sampled in one direction (parallel to the integral field slices described in Paper VI) by the detector pixels and in the orthogonal direction by the slices themselves. The detector scattering described above will therefore only apply in the along-slice direction of the photometric aperture. It will have a different effect in the dispersion direction, where it will cause light to be scattered outside the nominal spectral resolution element.

The magnitude of the impact on the MRS sensitivity is then determined by the size of the photometric aperture in the along-slice direction and the width of the spectral resolution element, both measured in pixels. The field of view of a single MRS pixel is $0.20''$ for $\lambda < 12$ μm (see Paper VI), a factor of 1.8 larger than that of the imager. In the spectral direction, the half-width of the spectral resolution element is roughly 0.9 pixels across this

FIG. 5.—Fraction of point source energy falling within the photometric aperture. The nominal case for the imager is shown as a *solid line*, and for the LRS as a *dashed line*. The *dotted lines* show the variations seen for the imager under the best and worst bounding cases of image quality.
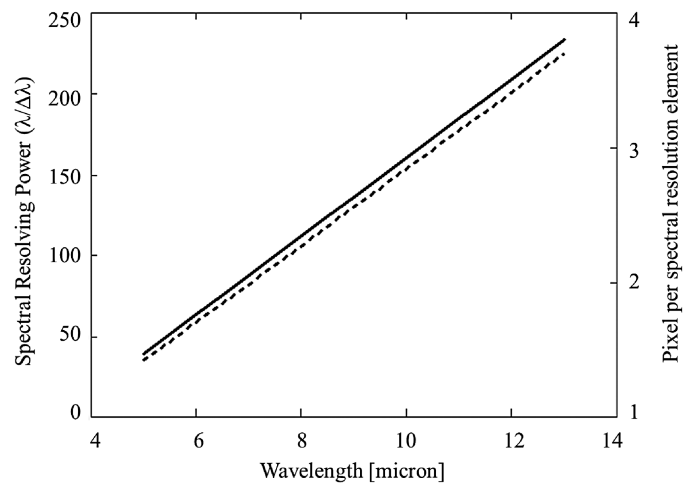

FIG. 6.—LRS spectral sampling parameters used in the sensitivity model. The spectral resolving power (*solid line*) and number of pixels per spectral resolution element (*dashed line*) are shown as a function of wavelength.
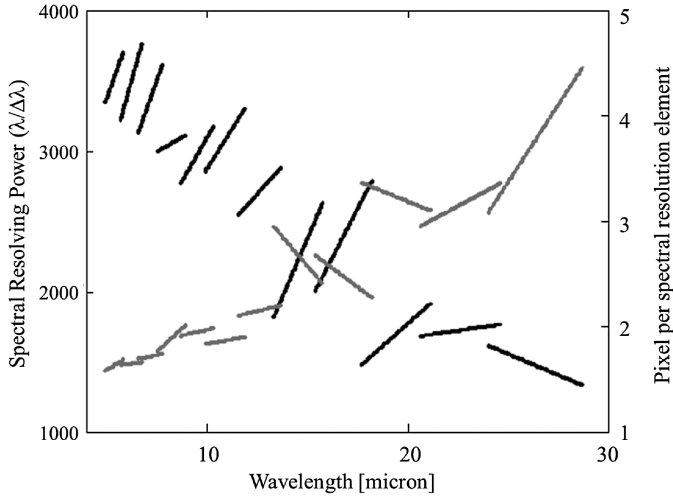
FIG. 7.—MRS spectral sampling parameters used in the sensitivity model. The spectral resolving power (*black line*) and number of pixels per spectral resolution element (*gray lines*) are shown as a function of wavelength.

spectral range (as shown in Fig. 7), a factor of 2.4 smaller than the diameter of the imager photometric aperture at $\lambda = 7$ μm. We therefore expect detector scattering to result in greater loss of signal for the MRS compared to the imager.

In the absence of a good understanding of the spatial distribution of detector scattering, we were unable to derive an accurate quantitative correction to $f_{\rm phot}$ for the MRS. Instead, inspection of the measured MRS PSF (specifically, Fig. 16 in Paper VI) suggests that we should increase the linear size of the photometric aperture by 50% in the along-slice direction to accommodate the observed extension, while leaving its across-slice dimension unchanged. For the sensitivity model, this is implemented by increasing $r_{\rm phot}$ by a factor of $\sqrt{1.5} = 1.22$ for the MRS. We note that this factor may prove to be conservative at long wavelengths ($\lambda > 10$ μm) where the along-slice extension should be reduced (irrespective of whether it is due to scattering in the detector or due to optical scattering at surfaces in the MRS).

2.4. Detector Performance

As described in more detail in Papers VII and VIII, the electrons generated in each pixel are used to charge a ~34 fF capacitor (with a 250,000 electron storage capacity in MIRI's case), which is sampled (read) multiple times at a fixed interval $t_{\rm frame}$. The photocurrent is then determined by finding the slope that best fits these samples, with a measurement error that includes terms due to the shot noise on the charge, the read noise associated with each sample, and the statistical effects of sampling up the ramp.

Analytical expressions that describe the signal and noise have been derived for example by Herter (1990), while Garnett and Forrest (1993) describe the terms that account for the sampling errors for the slope-fitting sampling scheme used by

MIRI. We have combined these to describe the signal and noise per pixel in a single integration in which the photocharge i, is integrated for a duration $t_{\rm int}$,

$$S_{\rm int} = i_{\rm sig} t_{\rm int}, \qquad (7)$$

$$N_{\rm int}^2 = k1(i_{\rm sig} + i_{\rm bgd})t_{\rm int} + k2 i_{\rm dark} t_{\rm int} + k3 R_N^2. \qquad (8)$$

Here, we separate the noise into three terms, which are related to: (1) the total incident photon flux, (2) the detector dark current (charge generated within the pixel in the absence of any illumination), and (3) the read noise per pixel on a single frame R_N. The constant factors in each term include the statistical effect of sampling the charge with $n_{\rm read}$ equispaced pixel reads (Garnett and Forrest 1993) as set out below,

$$k1 = k_{\rm exc} \frac{6}{5} \left(\frac{n_{\rm read}^2 + 1}{n_{\rm read}^2 - 1} \right), \qquad (9)$$

$$k2 = 1,$$

$$k3 = k_{RN{\rm obs}}^2 \frac{12 n_{\rm read}}{n_{\rm read}^2 - 1}.$$

We see that term $k1$ describes the factor by which the measured noise exceeds the theoretical shot noise limit under conditions where the signal from the astronomical target or the background dominate. The factor $k_{\rm exc}$ replaces the more familiar product of gain and gain dispersion (βG); as described in Paper VII, the detector model is consistent with values for β and G both being close to unity, but the detectors do exhibit noise which has been measured (Paper VII) during testing of the MIRI detectors to be significantly above the theoretical shot noise. For the sensitivity model, we use a value of $k_{\rm exc} = 1.3$.

Based on detector measurements, the noise associated with the dark current has been shown to follow Poissonian statistics (i.e., behave as shot noise), leading us to set factor $k2$ equal to unity. Dark current values of 0.12, 0.03, and 0.10 $e\,{\rm pixel}^{-1}\,{\rm s}^{-1}$ are adopted for the imager, short wavelength MRS and long wavelength MRS detectors, respectively.

For faint sources and low backgrounds, the factor $k3$ combines the ideal statistical reduction in the effective read noise compared to R_N with an additional factor $k_{RN{\rm obs}}$ (set equal to 1.23 [M. E. Ressler, private communication]), which reflects the measured factor by which the system noise falls short of this ideal behavior. The value of R_N is taken from Paper VIII as 32.6 electrons when the detector is operated in FAST mode. For SLOW mode, this is reduced by a factor of $\sqrt{8}$ to account for the 8 samples per pixel that contribute to each frame.

The per pixel photocurrents from the target and background ($i_{\rm sig}$ and $i_{\rm bgd}$ in eq. [8]) are then derived by application of equation (1) to the relevant illumination source. For the special case of the (continuum) background spectrum seen by the LRS, the solid angle subtended by a single imager pixel (0.11×0.11 arcsec^2)
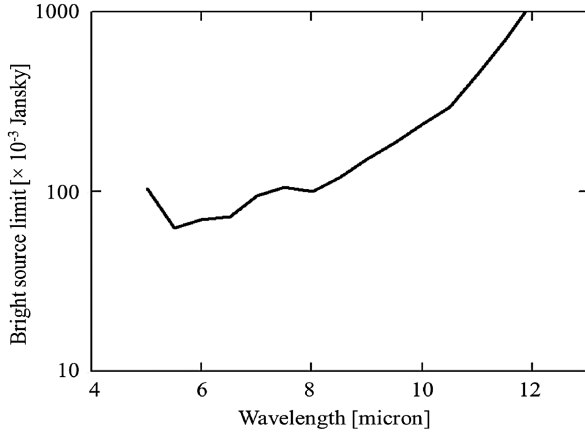
FIG. 8.—Bright source limits (calculated for the high background case only) for the MIRI Low-Resolution Spectrometer. The minimum value is 63 milli-Jansky at $\lambda = 5.5$ μm.

is scaled by a factor of 4.6 to account for the fact that each pixel in the LRS spectrum will see the coadded background from all (4.6) pixels across the slit. The wavelength-dependent fields of view of the four MRS spectral channels are specified in Paper VI.

There are several other factors that contribute to the sensitivity model. These include an efficiency factor that accounts for measurements that are lost due to the impact of cosmic rays. The effect of bad pixels and cosmic rays is currently folded in with the estimation of the effective exposure time $t_{\rm eff}$ that contributes to the integration for an exposure of duration $t_{\rm exp}$,

$$t_{\rm eff} = f_{\rm goodEOL} t_{\rm exp} (1 - R_\gamma t_{\rm int} - 1/n_{\rm read}). \qquad (10)$$

Here, R_γ ($=4.7 \times 10^{-4}$ s^{-1}) is the estimated rate at which pixels will be disrupted by cosmic ray impacts on orbit, and $f_{\rm goodEOL}$ ($=95\%$) is the fraction of pixels expected to be remaining in an operable state at the end of mission life. The final term uses $n_{\rm read}$, the number of up-the-ramp reads in an integration to account for the time lost between the reset and the first frame of the next integration.

It should be noted that this approach to cosmic ray events is somewhat conservative, since it assumes that the entire integration ramp is lost. In practice, the slopes before and after an event can be recovered using algorithms developed by the MIRI team (Gordon et al. 2014, Paper X).

3. MODEL PREDICTIONS

3.1. Bright Source Limits

We express the flux of a bright astronomical target as,

$$F_{bright} = \frac{i_{bright} - i_{bgd}}{f_{br\_pix} g}. \qquad (11)$$

Here, $i_{\rm bright}$ is the maximum acceptable photocurrent from a bright astronomical target, defined as that which will fill the brightest pixel in the image to 150,000 electrons (60% of the storage capacity quoted above) in the 5.6 s taken for the shortest useful full frame integration (comprising a reset and two "FAST" mode reads, as defined in Paper VIII). This equates to $26,800$ e s^{-1} pixel^{-1}.

The factor $i_{\rm bgd}$ accounts for the photocurrent generated by the background, which for the worst case of the F2550W filter and the "high-background" case defined above is estimated to be around 5100 e^{-1} s^{-1}. The factor g is then the end-to-end gain from astronomical target to photocurrent (with units of e s^{-1} Jansky^{-1}). This is calculated as a by-product of the sensitivity model using the PCE curves derived above and accounting for the relevant encircled energy and sampling factors. The target spectral shape is modeled as a 5000 K black body.

The factor $f_{\rm br\_pix}$ in equation (11) describes the fraction of the total signal from a point target that will fall in the brightest pixel. For the imager, based on analysis of model PSFs, we set $f_{\rm br\_pix\_imager} = 0.13$ for $\lambda \leq 8$ μm. At longer wavelengths, to allow for image dilution by diffractive broadening we use,

$$f_{\rm br\_pix\_imager} = 0.13(8 \ \mu{\rm m}/\lambda)^2. \qquad (12)$$

The resulting bright source limits (calculated for the high-background case) are then tabulated in Table 3. If the imager subarrays are used, then the limits shown in Table 3 should be increased by a factor equal to 2.78 s divided by the subarray frame time listed in Paper VIII. For example, the SUB64 subarray's 0.085 s frame time should allow a 0.4 Jansky target to be observed using the F560W filter without saturating.

For the LRS, where the PSF is coadded along the dispersion direction, we use $f_{\rm br\_pix\_lrs} = 0.36$ (the square root of the value used for the imager) for $\lambda \leq 8 \mu$m and for $\lambda > 8$ μm,

TABLE 3

LIMITING FAINT SOURCE DETECTION LIMITS (10σ IN 10,000 S) AND BRIGHT SOURCE LIMITS FOR THE MIRI IMAGER

Filter	Low-background detection limit (μJy)	High-background detection limit (μJy)	Brt. src. limit (mJy) full frame	Brt. src. limit (Jy) 64×64 subarray
F560W	0.16	0.16	13	0.42
F770W	0.25	0.25	7.4	0.24
F1000W	0.54	0.56	16	0.52
F1130W	1.35	1.43	69	2.25
F1280W	0.84	1.00	29	0.95
F1500W	1.39	1.94	37	1.23
F1800W	3.46	4.87	66	2.2
F2100W	7.09	9.15	66	2.2
F2550W	26.2	30.8	192	6.4

NOTE.—Note that the detection limits are quoted in micro-Jansky and the bright source limits (which are calculated for the high-background case only) are quoted in milli-Jansky and Jansky.

FIG. 11.—MRS limiting sensitivity for the detection of the continuum spectrum for a spatially unresolved target (units of milli-Jansky). The *dashed lines* are for the high-background case. See the electronic edition of the *PASP* for a color version of this figure.
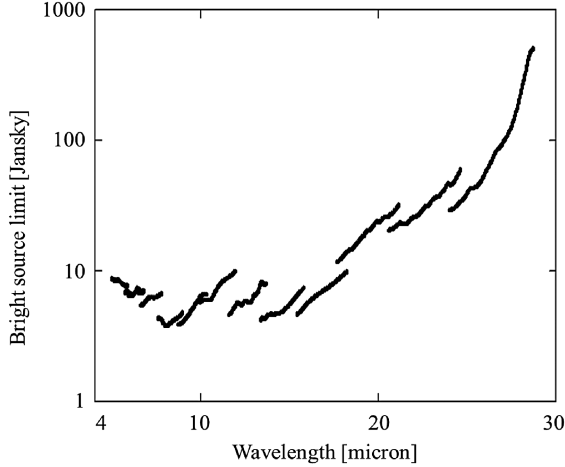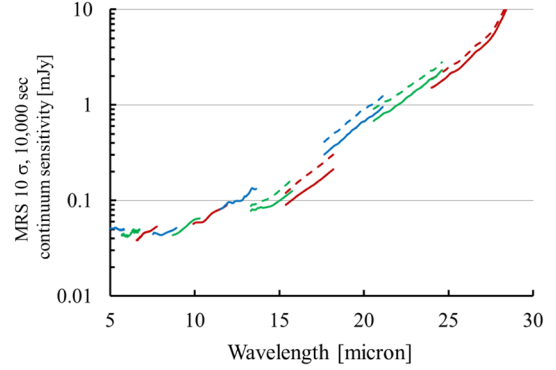
FIG. 9.—Bright source limits (calculated for the high background case only) for the MIRI Medium-Resolution Integral Field Spectrometer. The minimum value is 3.8 Jansky at $\lambda = 8$ μm.

$$f_{\text{br\_pix\_LRS}} = 0.36(8\ \mu m/\lambda) \tag{13}$$

The resulting bright limits are plotted in Figure 8. As for the imager subarrays, if the "SLITLESSPRISM" subarray with its 0.16 s frame time is used, then the limits should be increased by a factor of 17.

For the MRS, we scale $f_{\text{br\_pix\_imager}}$ by the ratio of the solid angle viewed by each MRS pixel to the solid angle viewed by an imager pixel. The resulting bright source limits are plotted in Figure 9. We note that the nominal MRS readout pattern currently uses "SLOW" mode (as defined in Paper VIII). If "FAST" mode is not implemented for the MRS on orbit, the MRS bright source limits presented here should be reduced by a factor of ~10.

3.2. Sensitivity

We can now write the formula used to calculate the limiting sensitivity, defined as the target flux needed to achieve a S/N ratio of 10 in a 10,000 s observation:

$$F_{\text{sens}} = 10k_{\text{margin}}k_{\text{extr}}k_{ff} \frac{F_{\text{point\_tgt}}}{(S_{\text{int}}/N_{\text{int}})\sqrt{N_{\text{phot}}\frac{t_{\text{eff}}}{t_{\text{int}}}}}. \tag{14}$$

Here, we introduce the term k_{ff} to account for the error due to differences in the gain of the individual pixels which are not corrected by standard division by a reference pixel flat (and which we refer to as flat fielding noise). We calculate its contribution to scale with the total signal collected as:

$$k_{ff} = 1 + K_{ff}\sqrt{\frac{t_{\text{eff}}}{t_{\text{int}}}(i_{\text{tot}}t_{\text{int}})}. \tag{15}$$

The factor K_{ff} is set equal to 10^{-3} for the spectrometer, 10^{-5} for the imager at $\lambda > 12$ μm, and 10^{-4} in all other cases. The

FIG. 10.—MRS limiting sensitivity for the detection of an unresolved spectral line in a spatially unresolved target (units of 10^{-20} Watt m^{-2}). The *dashed lines* are for the high-background case. See the electronic edition of the *PASP* for a color version of this figure.
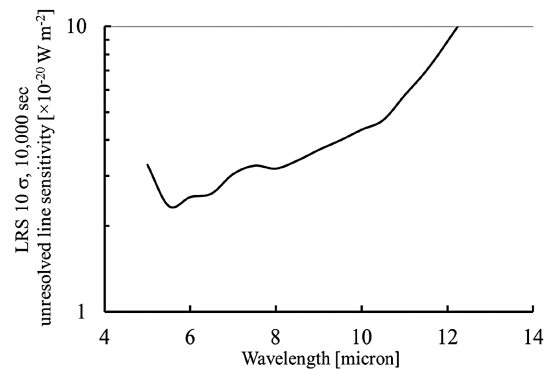

FIG. 12.—LRS limiting sensitivity for the detection of a spectrally and spatially unresolved target (units of 10^{-20} Watt m^{-2}).
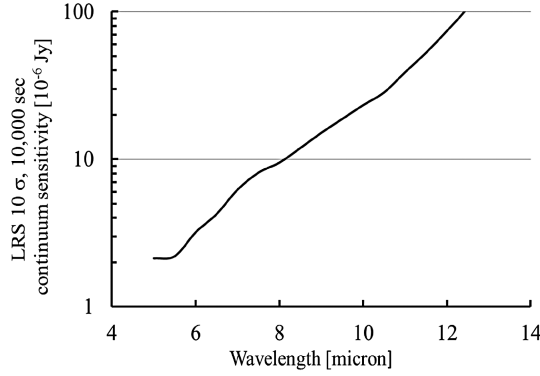
FIG. 13.—LRS limiting sensitivity for the detection of the continuum spectrum for a spatially unresolved target (units of microJansky).

factor k_{extr} is used to account for the noise penalty associated with extracting source fluxes from data which is not fully (Nyquist) sampled. On this basis, for MIRI it is set equal to 1.1 for the F560W imager filter and the MRS and equal to 1.0 in all other cases. Finally, we retain a factor k_{margin} (=1.1) to account for unexpected impacts on the delivered sensitivity that may arise before MIRI starts operation on orbit.

Table 3 lists the limiting sensitivities for each filter in the imager. For the MRS, Figure 10 plots the sensitivity for the detection of a spectrally unresolved emission line in a spatially unresolved target, with units of Watt m^{-2}, while Figure 11 plots the sensitivity for a spatially unresolved continuum source. The equivalent plots for the LRS are shown in Figures 12 and 13.

To allow the MRS sensitivities to be calculated conveniently we have made second-order polynomial fits to the model predictions within each MRS sub-band for the case of unresolved spectral lines and the nominal (low) radiative background. These fits are of the form:

$$LF = Ax^2 + Bx + C, \qquad (16)$$

where LF is the minimum line flux (for an unresolved line from a point source) that can be detected at 10σ in 10,000 s of integration and $x = \lambda - \lambda_0$. The fit coefficients are provided in Table 4; in general they reproduce the detailed model results to within a few percent (a worst-case deviation of 13% is seen for sub-band 3A).

Similarly, the sensitivity of the LRS for an unresolved line from an unresolved source (Fig. 12) can be approximated by a sixth-order polynomial:

$$LF = [3.11 - 3.017x + 3.4296x^2 - 1.5523x^3 + 0.3488x^4 \\ - 0.03842x^5 + 0.001696x^6] \times 10^{-20} \text{ Wm}^{-2}, \qquad (17)$$

where x is (wavelength in μm) -5. This expression reproduces the plotted result to within about 5% and is valid from 5–12 μm.

The sensitivity figures for continuum targets can be calculated using the spectral resolving powers listed in Paper VI. For extended sources, we note that the area of the photometric aperture used in the model is 0.83 arcsec^2 at $\lambda = 10$ μm and scales as λ^2. To take a specific example, if we wish to know the MRS sensitivity for a spectral line from an extended source at $\lambda = 12.8$ μm , equation (16) allows us to calculate the unresolved sensitivity as 0.84×10^{-20} Watt m^{-2} We divide this figure by the aperture area (1.83 arcsec^2) to give a figure of 0.63×10^{-20} Watt m^{-2} arcsec^{-2}. In converting to continuum sensitivity, the LRS resolution can be taken to be

$$R = \lambda/\Delta\lambda = 24x + 40 \qquad (18)$$

with x defined as in the preceding paragraph.

TABLE 4

COEFFICIENTS OF SECOND-ORDER POLYNOMIAL FITS TO THE MODEL MRS SPECTRAL LINE SENSITIVITIES

MRS channel and sub-band	λ_0 μm	A $\times 10^{-20}$ Wm^{-2} μm^{-2}	B $\times 10^{-20}$ Wm^{-2} μm^{-1}	C $\times 10^{-20}$ Wm^{-2}
1A	5.4	0.0074	−0.2813	0.7947
1B	6.2	0.0859	−0.1035	0.6183
1C	7.2	−0.0521	−0.0061	0.5764
2A	8.2	0.0998	−0.0368	0.5269
2B	9.5	−0.0069	0.0567	0.5563
2C	10.9	0.0180	0.0373	0.5932
3A	12.6	0.0608	0.0427	0.8146
3B	14.5	0.0858	−0.0371	0.8219
3C	16.8	0.0231	0.1258	0.9892
4A	19.4	0.0563	1.0128	4.9055
4B	22.6	0.3769	2.3739	8.9771
4C($\lambda < 27.5$ μm)	25.5	1.6318	6.4678	17.5406
4C ($\lambda \geq 27.5$ μm)	27.9	19.9690	39.1702	50.1592

NOTE.—Presents the noise equivalent line intensity to achieve a signal to noise ratio of 10 in a 10,000 s observation), for the nominal (low) radiative background. The spectral coverages of the individual MRS subbands are provided in Paper VI.

4. CONCLUSION

The limiting sensitivities presented above describe the MIRI team's most accurate estimate of the performance that will be achieved on orbit, based on the best available test results and analysis. We note that the figures are not significantly different from expectations presented previously (for example, in Glasse et al. [2006]), with the notable exception of the worse than expected performance for Channel 4. The overall effect of updating the sensitivity model has been to replace factors assigned to areas of potential risk with parameters describing measured features of the instrument.

Remaining areas of uncertainty in the model are probably dominated by the *JWST* radiative background at long wavelengths; the high-background bounding scenario we present here should be conservative. Other effects, such as the potential need to use subarray readouts (see Paper VIII) to avoid saturating on the background will have a much smaller impact unless the observatory background is significantly higher (more than a factor of two) than the higher of the levels assumed here. The accuracy of the sensitivity predictions is estimated to be in the region $\pm 20\%$, substantially less than the error bars on the PCE plots in Figures 2 and 3.

We have confirmed that the performance of MIRI continues to promise to meet its ambitious science goals. In conjunction with the bright source limits, these revised sensitivity figures can be regarded as accurate enough to allow potential MIRI observers some confidence in starting to refine and focus their planned observing programmes.

REFERENCES

Boccaletti, A., et al. 2014, PASP, 127, 633, Paper V

Bouchet, P., et al. 2014, PASP, 127, 612, Paper III

Garnett, J. D., & Forrest, W. J. 1993, Proc. SPIE, 1946, 395

Glasse, A., Lee, D., Parr-Burman, P., Hayton, D., & Mazy, E. 2006, Proc. SPIE, 6265, 118

Gordon, K., et al. 2014, PASP, 127, 696, Paper X

Herter, T. 1990, IP, 30, 97

Lightsey, P. A., & Wei, Z. 2012, Proc. SPIE, 8442, 84423B-1

Ressler, M. E., et al. 2015, PASP, 127, 675, Paper VIII

Rieke, G. H., Ressler, M. E., Greene, T. P., Morrison, J., Sukhatme, K., Walker, H., Bouchet, P., Regan, M., et al. 2014, PASP, 127, 665, Paper VII

Wells, M., Pel, J.-W., Glasse, A.C.H., Wright, G.S., Azzollini, R., Beard, S., Brandl, B., Gaillie, A., et al. 2014, PASP, 127, 665, Paper VII

Swinyard, B. M., Rieke, G., Ressler, M., Glasse, A. C. H., Wright, G., Ferlet, M., & M., Wells 2004, Proc. SPIE, 5487, 785

Wright, E. 1998, ApJ, 496, 1

Wright, G. S., et al. 2014, PASP, 127, 595, Paper II